CrystEngComm

Accepted Manuscript

Journal Name CrystEngComm Dynamic Article Links ►

Cite this: DOI: 10.1039/c0xx00000x

www.rsc.org/xxxxxx

ARTICLE TYPE

3D Hetero-architecture of GdB_6 nanoparticles on lessened cubic Cu_2O nanowires: enhanced field emission behaviour

Sachin R. Suryawanshi,[a] Anil k. Singh,[b] Meenal Deo,[c] Dattatray J. Late,[c] Sucharita Sinha,[b]* Mahendra A. More,[a]*

Received (in XXX, XXX) Xth XXXXXXXXX 20XX, Accepted Xth XXXXXXXXX 20XX
DOI: 10.1039/b000000x

The field emission properties (FE) of heteroarchitecture comprised of Gadolinium hexaborides nanoparticles uniformly decorated over Cu_2O nanoneedles (GdB_6/Cu_2O) have been investigated at the base pressure of ~ 1×10^{-8} mbar. Under the optimized pulsed laser deposition (PLD) well adherent coating of GdB_6 nanoparticles on chemically synthesized cuprous oxide (Cu_2O) nanoneedles has been obtained. A plausible growth mechanism of the hierarchical assembly of GdB_6 nanoparticles on the Cu_2O nanoneedles is explained on the basis structural analysis carried out using SEM and TEM. A low turn-on field of ~2.3 V/μm (to draw an emission current density ~ 1 μA/cm^2) is observed along with stable emission current at the preset value of ~2 μA over 4 h. The enhanced emission behaviour of the GdB_6/Cu_2O heteroarchitecture, in contrast to the pristine Cu_2O nanoneedles, is attributed to its high aspect ratio and low work function. The observed FE results demonstrate GdB_6/Cu_2O heteroarchitecture as a potential candidate for application in various vacuum nano/microelectronic devices.

1. Introduction

Rare earth hexaborides, owing to their unique set of physico-chemical properties such as low work function, high electrical conductivity, high melting point, low vapour pressure, mechanical, and chemical stability at high temperatures, have been extensively used for fabricating electron sources, both thermionic and field emitters, for practical applications in various vacuum electronic devices.[1-6] In the context of field emission (FE), the one-dimensional (1D) nanoforms are the preferred nanovariants, since their high aspect ratio offers unprecedented advantages in terms of lowering of the applied voltage range and relaxation of the operational base pressure.[7-9] In this regard, attempts have been made by various researchers to synthesize nanoforms such as nanocrystals, nanorods, nanowires, etc. of rare earth metal hexaborides and explore their FE characteristics.[1,2,4,10,11] Our group has reported FE characteristics of nanocrystalline thin films of LaB_6 on various refractory metal substrates synthesized by optimized Pulsed Laser Deposition (PLD) route.[12-14] L. Wang et. al. have presented a brief review on synthesis and characterization of rare earth hexaborides nanostructures.[15] Chemical vapour deposition of single crystalline GdB_6 nanowires and their FE properties have been studied by H. Zhang et. al.[1] The authors have observed that the GdB_6 nanowires emitter exhibits five-time larger emission current than that of the LaB_6 nanowires, when measured under identical conditions. Similarly, fabrication of vertically aligned single-crystalline LaB_6 nanotubes, nanowires and their FE behaviour has been reported by J. Xu et. Al.[16]

Although these attempts are scientifically meaningful and important, their technological applications are unconvincing, due to (a) The nanostructures obtained by the researchers are not 'well defined' similar to other 1D nanostructures of ZnO, Cu_2O, Si, CNTs, etc, (b) Their yield is seen to be poor (c) The synthesis methods involve complexity, toxic chemicals and high temperature.

From application point of view, for fabrication of cold cathodes based on nanostructures, two parameters viz, the aspect ratio and work function are very important. It is desirable that the nanostructures should have high aspect ratio and low work function. The rare earth hexaborides have lower work function but synthesis of their 'well' defined 1D nanostructure involves complexity. In contrast, synthesis of 'well' defined 1D nanostructure of metal oxides is facile; however their work function values are relatively higher. Therefore, there is scope to develop nanostructure emitters which will exploit low work function of rare earth hexaborides (RB_6) and the synthesis simplicity of 1D metal oxide nanostructures in synergic manner. Since FE is surface sensitive phenomenon, such 'desirable' emitters can be developed by growing a well adherent thin layer of rare earth hexaboride on 1D nanostructure of metal oxides. Cu_2O is a p-type direct band gap semiconductor (Eg~2.17 eV) having a good set of properties like, non-toxic, low cost, high chemical resistance, good thermal stability, etc. Being intrinsic p-type semiconducting material it can easily form a p-n junction and can be used in photovoltaic, H_2 production, water splitting, photocatalysis and photo-detector due to absorption in the

visible range.[17, 18]

Multifunctional metal oxide-rare earth hexaborides hybrid nanomaterials is a relatively new system in respect of other heterostructures such as ZnO-CeO_2, Cu_2O-ZnO, WO_3-SnO_2, SnO_2-Fe_2O_3, In_2O_3-SnO_2, Ag-ZnO, n-ZnO/p-AlGaN that have been investigated by various researchers.[17,19-24] Although the field of multifunctional heteroarchitectures has progressed significantly during past few years, the synthesis of metal oxide-rare earth hexaborides nanostructures is hitherto a challenge. In the present studies, we report synthesis of a 3D heteroarchitecture comprised of GdB_6 nanoparticles on (lessened) cubic Cu_2O nanowires. Interesting the GdB_6/Cu_2O heteroarchitecture exhibits superior FE behaviour as compared to the pristine Cu_2O nanoneedles. Furthermore, a plausible growth mechanism of the hierarchical assembly of GdB_6 nanoparticles on the Cu_2O nanoneedles is explained on the basis structural analysis carried out using SEM and TEM. The synthesis and FE investigation of GdB_6/Cu_2O heteroarchitecture reported herein is the first of its kind and to the best of our knowledge there are no such reports in the literature.

2. Experimental Section

2.1 Synthesis of Cu_2O/GdB_6 heteroarchitecture on copper substrate

The Cu_2O nanoneedles film was directly grown on the copper substrate by its anodization followed by annealing at 450 °C in controlled oxygen pressure ~ 5×10^{-6} mbar. For anodization, aqueous solution of 2M KOH was used as an electrolyte. A pre-cleaned high purity polycrystalline copper foil (5.0 cm × 1.0 cm × 0.1 mm) was used as a working electrode and a graphite rod as a counter electrode. The anodization was carried out at a constant current density of ~8 mA/cm^2 for ~5 min. After anodization, formation of evenly widen $Cu(OH)_2$ nanoneedles film was observed on the Cu substrate, which on annealing at ~450 °C under controlled oxygen environment (O_2 partial pressure~ 5×10^{-5}) got converted into Cu_2O nanoneedles. The synthesis of GdB_6 nanostructures on these Cu_2O nanoneedles was done by Pulsed Laser Deposition (PLD) technique. The deposition was carried out at the base pressure of ~ 1×10^{-5} mbar and substrate temperature of ~ 400 °C. For PLD, a second harmonic of Q-switched Nd:YAG nanosecond laser (λ = 532 nm, pulse duration ~ 10 ns, and 10 Hz repetition rate) was used to ablate a GdB_6 pellet (diameter ~ 10 mm, thickness ~ 5 mm). The GdB_6 pellet was prepared from high purity GdB_6 powder (purity 99.99%, Sigma Aldrich Chemicals) with poly vinyl alcohol as a binder, applying a pressure of ~80 kN/cm^2 followed by sintering under Argon ambience at ~700 °C for 4 hours. The substrate and target were held parallel to each other with separation of ~ 5.5 cm. Scheme 1 depicts a chart of the synthesis of Cu_2O nanoneedles and GdB_6 nanostructures on these needles.

In order to reveal the influence of PLD process variables, the synthesis was carried out at different laser fluence, number of pulses (ablation duration) and substrate temperature, keeping the other parameters constant. Furthermore, from the SEM analysis of the as-synthesized products, a plausible explanation pertaining to growth of the GdB_6 nanoparticles on the Cu_2O nanoneedles has been presented.

2.2 characterizations

The surface morphology of the as-synthesized Cu_2O nanoneedles and GdB_6/Cu_2O heteroarchitecture was examined using scanning electron microscope (SEM, JEOL 6360A) and field emission scanning electron microscope (FE-SEM, Hitachi S4800). The phase identification of the as-synthesized products was obtained by X-ray diffractometer (XRD, D8 Advance, Bruker AXS). For detailed morphological and structural analysis transmission electron microscope (TEM, Tecnai G^2 U20 FEI) was used. For TEM studies, the Cu_2O and Cu_2O/GdB_6 heteroarchitecture were scratched-off the substrate surface. The powdered material thus obtained was dispersed in analytical grade acetone by ultrasonicating for 5 min. A drop of the ultrasonicated dispersion was put onto a TEM grid. Furthermore, chemical analysis of the GdB_6/ Cu_2O heteroarchitecture was performed on X-ray Photoelectron Spectrometer (XPS, VG Microtech ESCA 3000).

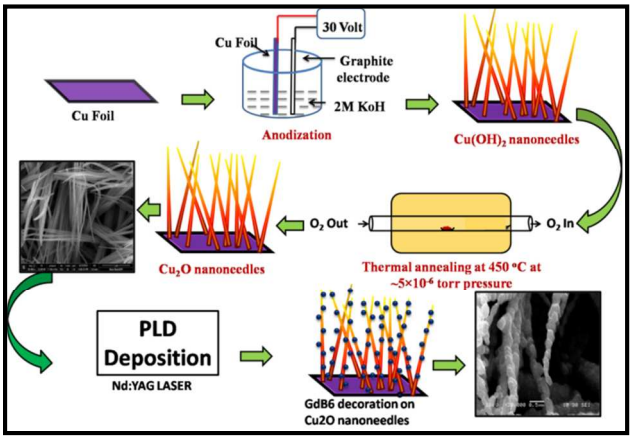

Scheme 1 Schematic of the growth procedure of GdB_6/Cu_2O heteroarchitecture

Field emission

The field emission studies of the Cu_2O nanoneedles and GdB_6/Cu_2O heteroarchitecture emitters were carried out in a planar 'diode' configuration at base pressure of ~1.0×10^{-8} mar. A typical 'diode' configuration consists of semitransparent phosphor screen (diameter ~ 40 nm) as an anode and the as-synthesized products as cathode. The cathode (Cu_2O nanoneedles grown on Cu foil, and the GdB_6/Cu_2O heteroarchitecture grown on Cu foil one at a time) was pasted on a stainless steel holder (diameter ~ 4.5 mm) connected to a linear motion drive. All FE measurements were performed at constant separation of ~1 mm, between the anode and cathode. The emission current was measured on Keithely Electrometer (6514) by sweeping dc voltage applied to cathode with a step of 40 V (0-40 kV, Spellman, U.S.) The field emission current stability was recorded at different preset current values. Special care was taken to avoid leakage current using shielded cables and ensuring proper grounding. Before recording the FE measurements, pre-conditioning of the cathode was carried out by keeping it at ~3 kV for 60 minutes, so as to remove loosely bound particles or contaminants by residual gas ion bombardments. The reproducibility of the FE results was checked for two samples synthesized under identical conditions.

3. RESULT AND DISCUSSION

3.1 Structural studies

A typical XRD pattern of the GdB_6/Cu_2O heteroarchitecture (Fig.1) exhibits a set of well defined diffraction peaks implying its crystalline nature. The observed diffraction peaks could be indexed to the GdB_6 (JCPDS card, No# 24-1056) and Cu_2O phases (JCPDS card, No# 125678-2076). Interestingly the XRD pattern does not show diffraction peak(s) corresponding to the CuO or other phases, indicating high purity of the as-synthesized product. Thus, the XRD analysis clearly reveals formation of high purity crystalline GdB_6/Cu_2O heteroarchitecture phase under the prevailing experimental conditions.

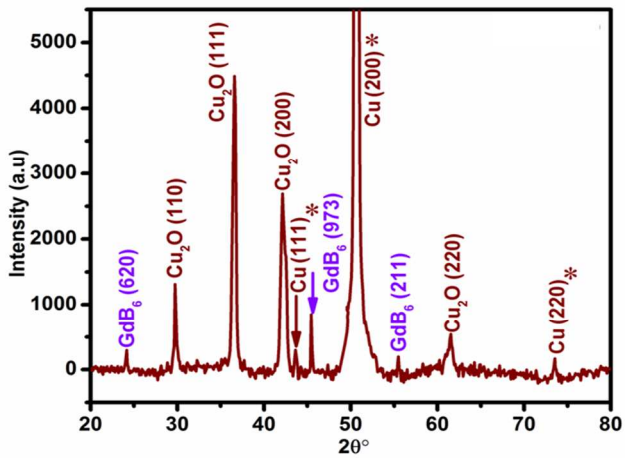

Fig 1. XRD pattern of the GdB_6/Cu_2O heteroarchitecture * represent copper substrate peaks.

3.2 Surface Morphology

The panoramic morphologies of the as-synthesized Cu_2O nanoneedles and GdB_6/Cu_2O heteroarchitecture obtained using FESEM and SEM are depicted in Fig. 2. The SEM images (Fig. 2a and 2b), indicate the formation of spine like nanostructures of Cu_2O with average base diameters of ~80-120 nm, upon anodization of Cu foil into 2M KOH followed by annealing at ~450°C under controlled oxygen environment. The micrographs reveal that the spine-like nanostructures are composed of self-assembled Cu_2O nanoneedles uniformly covering the entire substrate surface. The low magnification SEM images of the GdB_6/Cu_2O heteroarchitecture exhibit identical morphology as that of Cu_2O nanoneedles implying no significant change in shape and size of the nanostructures during PLD of GdB_6. However, a careful observation of the high magnification SEM images (Fig. 2c-f) reveals presence of tiny GdB_6 nanoparticles (average size ~ 150 nm) uniformly decorating the Cu_2O nanoneedles.

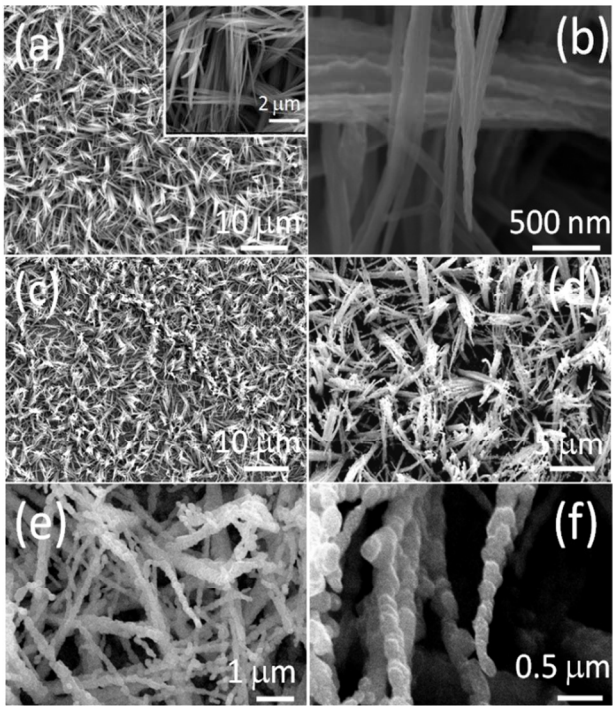

Fig.2 FESEM images of as-synthesized Cu_2O nanoneedles (a and b) SEM image of GdB_6/Cu_2O hetero-architecture in fig (c-f)

3.3 TEM Analysis

In order to gain further understanding of the structural and crystallographic features TEM observations were carried out. Fig.3a depict a bright field TEM image of as-synthesized Cu_2O nanoneedles, with base diameter ~90 nm and very fine apex, complementing the SEM results. The lattice-resolved HRTEM image of single Cu_2O nanoneedles (Fig. 3b) clearly reveals its crystalline nature. A single distinct fringe pattern with 'd' spacing of ~0.24 nm, is observed in the image, which correspond to the (111) lattice plane of Cu_2O cubic phase. Furthermore, the selected area electron diffraction (SAED) pattern, depicted as inset of Fig. 3a, confirms single crystalline nature of the Cu_2O nanoneedle. The bright field TEM image of GdB_6/Cu_2O heteroarchitecture (Fig. 3c) shows presence of GdB_6 nanoparticles on the Cu_2O nanoneedles. A slight increase in the diameter of Cu_2O nanoneedles in this case is due to presence of the GdB_6 nanoparticles. An average size of the GdB_6 nanoparticles measured from TEM analysis is estimated to be ~50 nm. Fig. 3d depicts the lattice-resolved HRTEM image of the heteroarchitecture recorded from its edge, which exhibits two distinct fringe patterns, one with 'd' spacing of ~ 0.20 nm corresponding to the (973) lattice plane of GdB_6 cubic phase (inset of Fig. 3(d))and another with 'd' spacing of ~ 0.24 nm (inset of Fig. 3(b)), characteristics of the (111) plane of the Cu_2O phase. Interestingly, the SAED pattern of heteroarchitecture sample (inset of Fig. 3c) shows combination of spots and rings, which is due to diffraction from two phases (GdB_6 and Cu_2O). Thus the TEM analysis clearly reveals crystalline nature of the heteroarchitecture. Furthermore, the EDAX spectrum of the heteroarchitecture (supporting information Fig.S1) shows presence of Cu, O, Gd and B species, in the GdB_6/Cu_2O heteroarchitecture on Cu foil under the

prevailing experimental conditions.

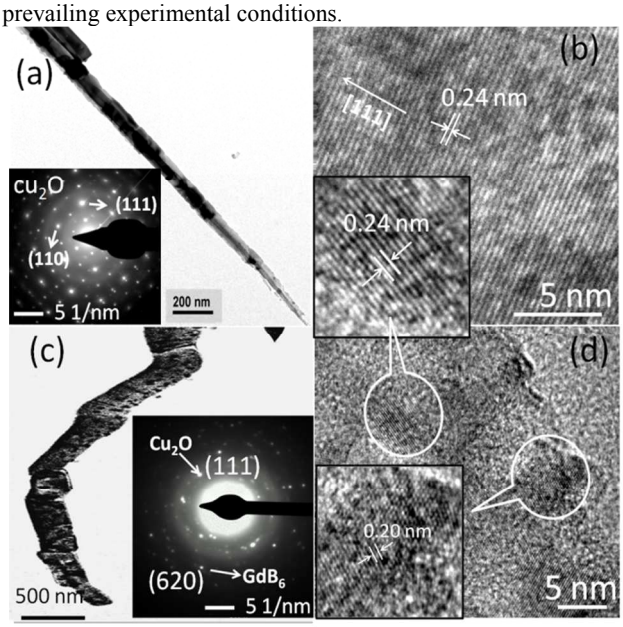

Fig 3. TEM images of the GdB_6/Cu_2O nanocomposite. (a) Low magnification bright field image with inset shows the SEAD pattern (b) HRTEM image of a single Cu_2O nanoneedle with inset shows the magnified HRTEM image of Cu_2O (c) Low magnification bright field image of GdB_6/Cu_2O heteroarchitecture with the corresponding SEAD pattern depicted as inset **(d)** HRTEM image of GdB_6/Cu_2O heteroarchitecture with inset shows magnified HRTEM GdB_6.

3.4 Growth mechanism

In order to reveal the influence of PLD process variables and understand the growth mechanism of coalition of the GdB_6 nanoparticles on Cu_2O nanoneedles, the synthesis experiments were performed employing different values of laser fluence, substrate temperature, and duration, as tabulated in Table 1. Based on the SEM analysis, we herein propose the fluence, temperature and time dependent growth model of the GdB_6 nanoparticles on the Cu_2O nanoneedles.

When the deposition was attempted at laser fluence of ~ 3 J/cm^2, substrate temperature ~ 200 ^{o}C for 5 minutes duration, the FESEM image (Fig. 4a) revealed presence of very few GdB_6 nanoparticles preferentially on the tips of Cu_2O nanoneedles. It suggests that the amount of vapour generated from the target followed by its condensation on the nanoneedles is not enough to cover the entire surface of the Cu_2O nanoneedles, and hence either laser fluence or deposition duration should be increased. With the increase in deposition time (10 minutes), presence of tiny nanoparticles on surface of the nanoneedles was observed (Fig. 4b). The SEM images revealed increase in areal density of the GdB_6 nanoparticles with increase in the deposition duration. In order to obtain more areal density with uniform coverage of the GdB_6 nanoparticles, an attempt was made at higher substrate temperature. However, in this case, the SEM analysis showed no appreciable change in the morphology as well as density of GdB_6 nanoparticles (Fig. 4c), with respect to the earlier case. So, it was decided to vary (increase) the laser fluence to obtain desirable growth and morphology of the GdB_6 coating. Interestingly, at higher laser fluence of 6 J/cm^2, (substrate temperature ~ 200 ^{o}C, deposition durations ~ 10 min) well adherent coating of GdB_6 nanoparticles uniformly covering the entire surface was observed, as seen in Fig. 4d. The GdB_6 nanoparticles are characterized with smooth surface, with an average size of ~ 50 nm. With further incresed in the substrate temperature (~ 400 ^{o}C) and deposition duration (20 minutes), the GdB_6 nanoparticles are observed to coalesce to form bigger nanoparticles characterized by faceted morphology as seen in Fig.4e. The average size of the nanoparticles is estimated to be ~150 nm. It is speculated that at higher substrate temperature, thermally activated diffusion of the GdB_6 vapour on the substrate surface takes place resulting into their coalescence. The formation of irregular shaped facetted structures during coalescence of the smaller nanoparticles may be attributed to minimization of the surface energy of the resultant product. The formation of well adherent GdB_6 nanoparticles at higher laser fluence (6 J/cm^2) is due to the fact that the standard heat of formation of GdB_6 (- 133.99 KJmole^{-1}) is larger than any other phase. Fig. 4(f) shows the schematic presentation of typical Gdb_6/Cu_2O heteroarchitecture sysytem.

Lattice mismatch is known to play a significant role in the epitaxial growth of Cu_2O/GdB_6 heterogeneous structures obtained *via* PLD, gas-phase, electrochemical, solution phase conformal epitaxial growth. A high degree of lattice mismatch prevents the nucleation and growth of an over layer on a nanostructure due to presence of an appreciable structural strain. It should also allow the selective growth of nanomaterials on a specific crystal surface of substrate material to facilitate novel architectures of heterogeneous nanostructures *via* the reasonable design and control of the growth environment.[25] Therefore, the (111) facet of Cu_2O nanoneedles, which possesses a better lattice match, is more favorable for the nucleation and growth of GdB_6 nanostructure.

Table 1 Different process variables of Pulsed Laser Deposition

Sample	Laser Fluence (J/cm^2)	Substrate temperature (^{o}C)	Deposition time (min)
(a)	3	200	5
(b)			10
(c)		300	10
(d)	6	200	
(e)		400	20

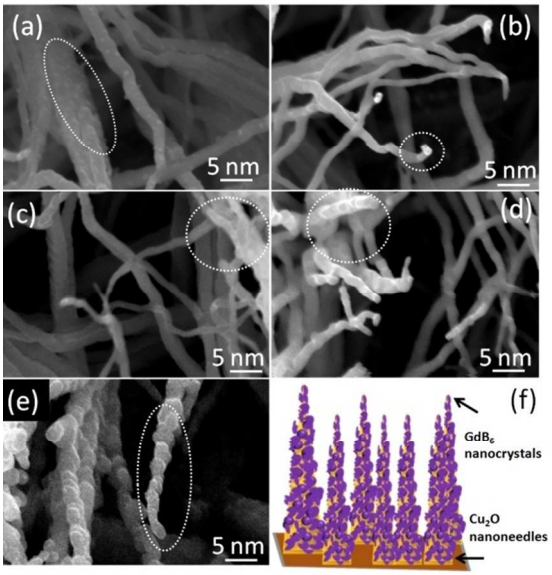

Fig. 4 (a-e) SEM images of PLD deposited GdB_6/Cu_2O nanoneedles at different process variables (f) schematic presentation of typical Gdb_6/Cu_2O heteroarchitecture sysytem.

3.5 XPS Analysis

Fig. 5a depicts a survey scan of the XPS spectrum of as-synthesized GdB_6/Cu_2O heteroarchitecture. The binding energy was corrected for specimen charging, through referencing the C 1s to 284.6 eV. The XPS spectrum depicts signatures of Cu, Gd, O and B only, in addition to the residual carbon, implying purity of sample. The survey scan (Fig. 5a) is further resolved to identify the energy levels corresponding to Cu, Gd, Band O.

The de-convoluted XPS scan of the Cu-2p level (Fig. 5b) exhibits peaks at 933.2 and 953.1 eV, which are characteristics of Cu-$2p_{3/2}$ and Cu-$2p_{1/2}$ levels, respectively and are is in good agreement with earlier reports.[25] The occurrence of a weak satellite signature at ~943.7 eV, on the higher binding energy side of the Cu-$2p_{3/2}$ peak is due to presence of dangling bonds like Cu-O on the surface. The 'weak' intensity of this satellite peak clearly exemplifies that the amount of CuO is minuscule. The de-convoluted O 1s scan, (Supporting information Fig. S2), exhibits two peaks of O $1s_{1/2}$ level, the main peak at energy of 530.9 eV is characteristic of CuO phase in crystal lattice formation in Cu_2O. The peak of 531.45 eV is ascribed to adsorbed oxygen on the surface of Cu_2O nanoneedles.[18] Fig. 5c shows the resolved XPS spectrum corresponding to Gd 4d energy level. The Gaussian fitted Gd-4d scan exhibits two well defined peaks of Gd at ~143 and ~ 148.02 eV, corresponding to the Gd-$4d_{5/2}$ and Gd-$4d_{3/2}$ energy states resulting due to spin orbit interaction in rare earth metal hexaboride. [26-28] Although XPS analysis is carried out under UHV environment, some impurities like oxygen can get incorporated in the sample, when exposed to ambient. Since the sample was not subjected to any cleaning/degassing treatment prior (during) to the XPS analysis, the physisorbed oxygen present in the sample gives rise to its characteristic signature at 531.45 eV in the observed spectrum. In addition a signature of B-1s $_{1/2}$ level is observed at 189.95 eV, as seen in Fig. 5d.

A carful observation of the survey scan reveals appearance of some weak intensity peaks due to Cu at ~84, 337 and 472 eV. The binding energies of Cu (LMM) are observed in the energy range 300 to 500 eV, which are attributed to the Auger photo-electron emission. Similar Auger photo-emission signature due to O (KVV) is also observed in the survey scan. The observed sub-binding energy peaks due to Auger emissions of Cu and O, are as described in XPS handbook.[29] Interestingly, no characteristic peaks due to other impurities were observed in the XPS spectrum. Thus the XPS results clearly indicate formation GdB_6/Cu_2O hetero-architecture phase under the prevailing experimental conditions.

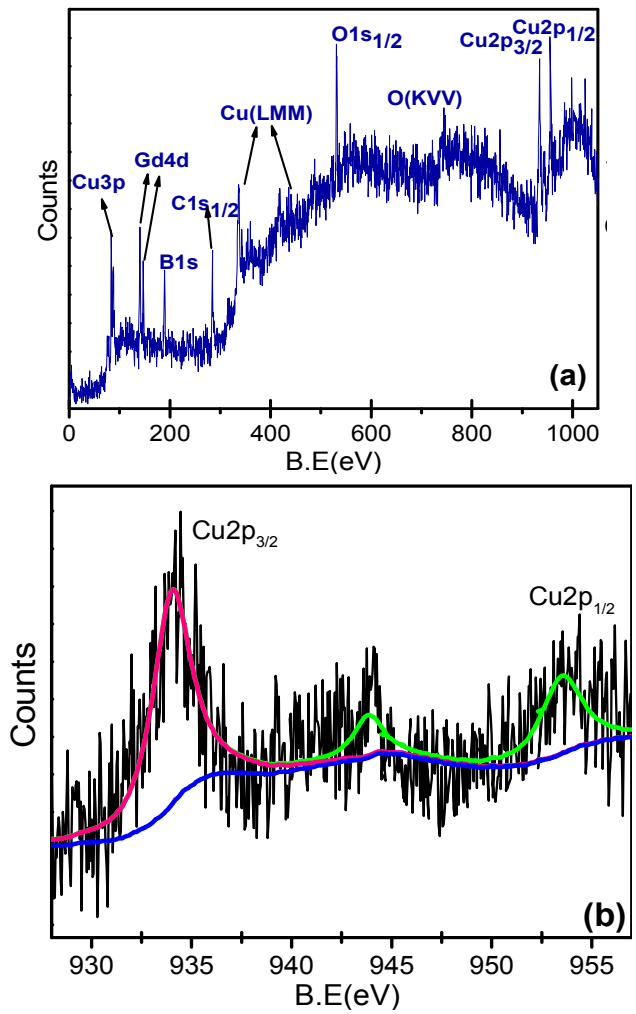

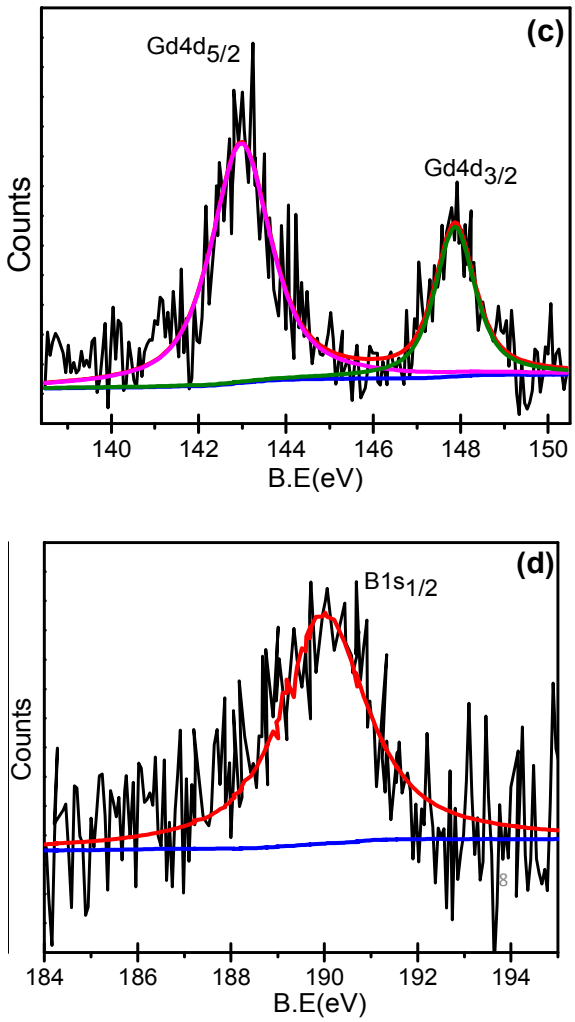

Fig. 5 XPS spectra of the GdB_6-Cu_2O hetero-architecture (a) a survey scan (b) $Cu2P_{3/2}$, $Cu2p_{1/2}$ state (c) $Gd4d_{5/2}$, $Gd4d_{3/2}$ states, (c) $B1s_{1/2}$ state

3.6 Field Emission

The FE reports on GdB_6 are limited in contrast to the other rare earth metal hexaborides and their heterostructures with metal oxides. Moreover, the possibility of enhancing FE characteristics of GdB_6 by making its composites with metal oxides has not yet explored. Fig. 6a depicts a plot of the emission current density versus applied electric field (*J-E* plot). The values of turn-on and threshold field, defined as the field required to draw an emission current density of ~1 μA/cm^2 and ~10μA/cm^2, are found to be ~3.25 V/μm and ~3.75V/μm, respectively for pristine Cu_2O nanoneedles, and ~2.3 V/μm and ~2.8 V/μm, respectively for the GdB_6/Cu_2O heteroarchitecture emitter. Furthermore, high emission current density of ~900 μA/cm^2 has been drawn from the GdB_6/Cu_2O heteroarchitecture emitter at an applied electric field of ~5.6 V/μm, in comparison to ~250 μA/cm^2 at an applied electric field ~5.6 V/μm, from the pristine Cu_2O nanoneedles emitter. The observed values of the turn-on and threshold field for the heteroarchitecture emitter are comparable to those reported for various rare earth metal hexaborides nanostructures and metal oxide heterostructures (complied in Table 2.). The observations of low turn on field and higher emission current density at relatively lower applied field can be attributed to unique geometrical form of the GdB_6/Cu_2O heteroarchitecture. In the case of such spine like structures, the applied field gets enhanced at the tips of Cu_2O nanoneedles, which successively acts as the 'applied' field for the GdB_6 nanoparticles. Furthermore, enhanced emission current density is attributed to the lower work function of the GdB_6 nanoparticles, present on the Cu_2O nanoneedles. Thus increase in the current density is due to the presence of GdB_6 nanoparticles on Cu_2O nanoneedles which acts as potential emission sites. From the basics of FE, the emission current density is mainly decided by the intrinsic property (work function) and extrinsic property (shape and size) of the emitter material. Thus, for better FE performance the material possessing low work function should be synthesized in quasi 1D form with sharp tapering apex, and preferably oriented perpendicular to the substrate i.e. vertically aligned. As revealed from the SEM and TEM images, the present GdB_6/Cu_2O heteroarchitecture meets the aforesaid requirements of a good field emitter. The GdB_6/Cu_2O heteroarchitecture exploits properties of its constituting counter parts in synergic manner. The high aspect ratio due to Cu_2O nanoneedles causes significant field enhancement, where as the low work function of GdB_6 (along with its nanometric form) facilitates enhanced emission of electron at low applied voltage. Furthermore, the electronic properties of the GdB_6/Cu_2O nanoneedle interface may play some role in enhancing the electron emission characteristic.

Table 2 Turn-on field values of GdB_6/Cu_2O hetero-architecture and various rare earth metal hexaborides nanostructure reported in the literature.

Sr. No	Morphology	Turn-on field (V/μm)	Threshold field (V/μm)	Ref.
1	GdB_6 single nanowires	10 nA at 650 V	150 nA/cm^2 at 3.2	1
2	CeB_6 nanowires	1 μA/cm^2 at 1.8	10 μA/cm^2 at 9.95	3
3	LaB_6 on W tip	1 nA at 1KV	100 μA at 7.2 KV	30
4	LaB_6 on W foil	1 nA at 1.2	2.86 at 2.16	12
5	Cu_2O/ZnO nano-brush	1 μA/cm^2 at 6.5	10 μA/cm^2 at 8.9	17
6	GdB_6/Cu_2O hetero-architecture	1 μA/cm^2 at 2.30	10 μA/cm^2 at 2.80	Present work

In the present investigation, the current density, J is defined as $J = I/A$, where I is the measured value of the emission current and A is the overall area of the emitter (~1 cm^2). The applied field (E) is defined as $E = V/d$, where V is the applied potential and d is the separation between the anode and the cathode. This field is also referred to as an average field.

The field emission characteristic is further analyzed by Fowler-Nordheim equation, which is given by, [31]

$$J = \left(\frac{AE^2\beta^2}{\varphi}\right)\exp\left(-\frac{\beta\varphi^{3/2}}{\beta E}\right) \quad (1)$$

Where, A=1.54 × 10^{-6} A eV V^{-2} and β= 6.83 × 10^3 $eV^{-3/2}$ V/ µm, J is the current density, E is the applied electric field, φ is the work function of emitting material and β is field enhancement factor. The Fowler-Nordheim (F-N) plot derived from the observed J-E characteristic is shown in Fig. 6b. The F-N plot shows an overall linear behaviour with decrease in the slope (non-linearity) in high field region. The field enhancement factor (β) is estimated from the slope (m) of the *F-N* plot using the following equation.[32]

$$\beta = \frac{-6.8\times10^3\,\phi^{3/2}}{m} \quad (2)$$

The estimated values of field enhancement factor (β) are observed to be ~1868 and ~2860 for Cu_2O nanoneedles and GdB_6/Cu_2O heterearchitecture emitters, respectively.

Along with the emission characteristics, current stability is one of the important parameters in the context of practical applications of cold cathodes. The emission current *versus* time (I-t) plots corresponding to pre-set value of ~5 µA for Cu_2O and GdB_6/Cu_2O heteroarchitecture recorded over a period of 3 hours (with sampling interval of 10 sec) at a base pressure of 1 × 10^{-8} mbar, are depicted in Fig. 6c and 6d. Fig. 6c shows that the emission current is almost stable for Cu_2O nanoneedles, whereas instabilities in the emission current is seen for GdB_6/Cu_2O heteroarchitecture emitter. The appearance of 'spike' type fluctuations in the emission current is attributed to (i) various atomic scale process such as adsorption, diffusion, desorption of residual gas species on the emitter surface. Furthermore, in case of planer emitter comprised of 1D nanostructures, extinction and generation of emission sites due to residual gas ion bombardment may contribute to instabilities in the emission current. Also the instability in emission current in GdB_6/Cu_2O heteroarchitecture can be attributed to the densely crowded GdB_6 nanoparticles which cause more surface area for the adsorption and diffusion of residual gas molecules on the emitter surface. These processes occurring on atomic scale lead to instantaneous change in the 'local' work function at the emission site, and thereby generating 'spike' in the emission current. The emission current stability is observed to be good, with fluctuations within ±10 % of the average value. An interesting feature of the GdB_6/Cu_2O heteroarchitecture cathode is that the average emission current remains constant over the entire duration and shows no signs of degradation of the emitter, indicating its good physical and chemical stability. The typical field emission images recorded during the stability measurements are depicted as inset of Fig. 6c and d. The FE images reveal that the GdB_6/Cu_2O heteroarchitecture has more number of emission sites as compared to the Cu_2O nanoneedles emitters, which implies that the emission is from the GdB_6 nanoparticles. The overall enhanced field emission behaviour exhibited by the GdB_6/Cu_2O heteroarchitecture put forth as a promising electron source for practical applications in various vacuum micro/nano electronic devices.

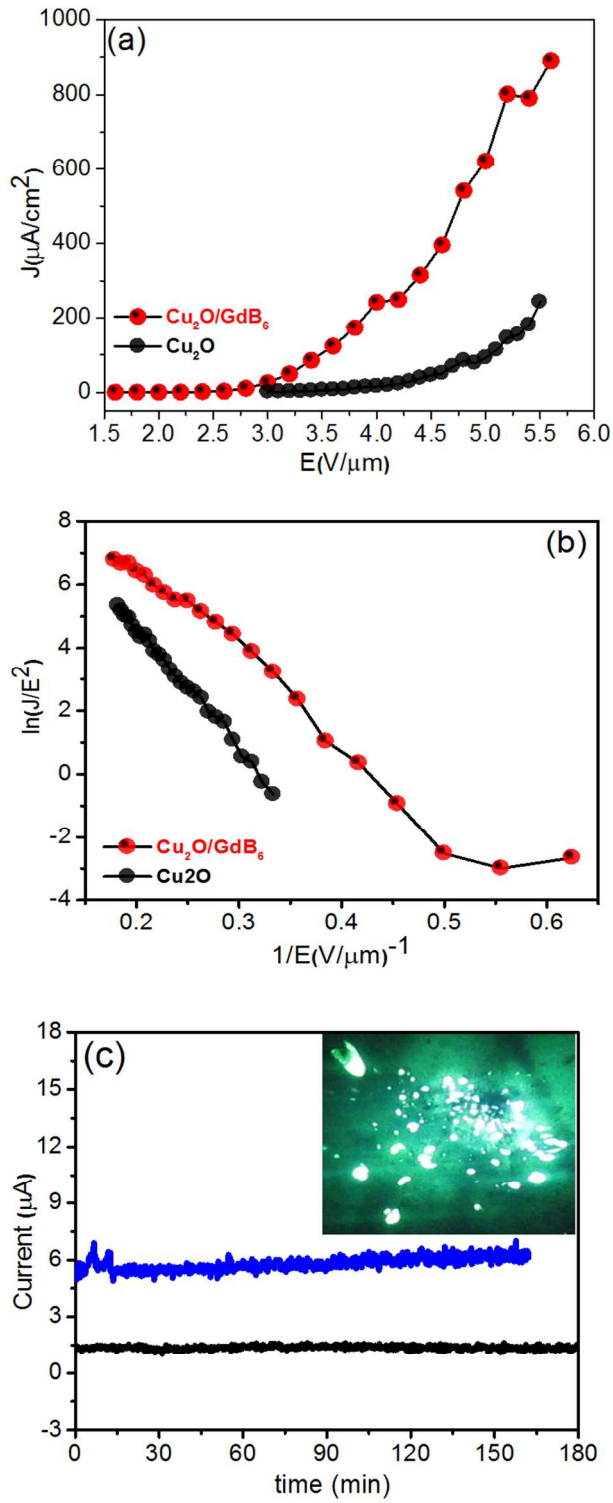

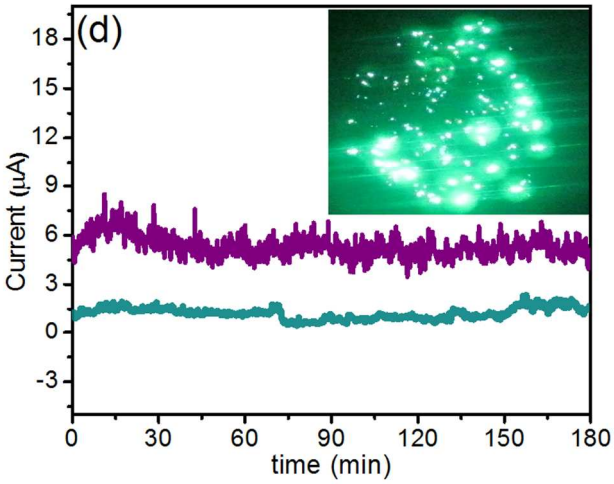

Fig. 6 Field emission characteristics of the Cu_2O nanoneedles and GdB_6/Cu_2O heteroarchitecture emitter (a) emission current density versus applied electric field (J-E) curve (b) Fowler-Nordheim (F-N) plot, (c) emission current versus time (I-t) plot with inset a typical field emission micrographs of Cu_2O nanoneedles (d) emission current versus time (I-t) plot with inset a typical field emission micrographs of GdB_6/Cu_2O nanoneedles

4. CONCLUSION

In conclusion, unique GdB_6/Cu_2O heteroarchitecture was synthesized using optimized pulsed laser deposition. The structural and morphology investigations reveal formation of the GdB_6/Cu_2O heteroarchitecture, comprised of self assembled Cu_2O nanoneedle uniformly decorated with faceted GdB_6 nanoparticles. The surface modification of Cu_2O nanoneedles due to GdB_6 nanoparticles leads to superior field emission behaviour, with a low turn-on field value ~ 2.3 V/μm (emission current density ~1 μA/cm^2) and delivery of ~ 900 μA/cm^2 at ~5.6 V/μm. The promising FE behaviour of the GdB_6/Cu_2O heteroarchitecture is attributed to synergic exploitation of the high aspect ratio due to Cu_2O nanoneedles and low work function of GdB_6, along with its nanometric form.

Acknowledgments

Mr. Sachin Suryawanshi gratefully acknowledges the financial support from BARC, Mumbai, for the award of Senior Research Fellowship under BARC-UoP memorandum (Grant No: GOI-E-153). MAM would like to thank the BCUD, Savitribai Phule Pune University, India for the financial support provided for the field emission work under CNQS-UPE-UGC program activity.
The author SRS would like to thank Prof. S. B. Ogale and Prof. Dilip S. Joag for encouragement and useful discussions during the investigation. The research work was supported by Department of Science and Technology (Government of India) for Ramanujan Fellowship to Dr. D. J. Late (Grant No. SR/S2/RJN-130/2012), NCL-MLP project grant 028626, DST-SERB Fast-track Young scientist project Grant No. SB/FT/CS-116/2013 and the partial support by INUP IITB project sponsored by DeitY, MCIT, Government of India.

[a]*Centre for Advanced Studies in Materials Science and Condensed Matter Physics, Department of Physics, Savitribai Phule Pune University, Pune 411007, India*
[b] *Laser & Plasma Technology Division, Bhabha Atomic Research Centre, Trombay, Mumbai 400 085, India*
[c] *National Chemical Laboratory (NCL-CSIR), Dr. Homi Bhabha Road, Pune 411008, India*
*E-mail- mam@physics.unipune.ac.in
*E-mail- ssinha@barc.gov.in

Notes and references

1 H. Zhang.; Q. Zhang.; G. Zhao.; J. Tang.; Q. Zhou.; L. C. Qin., *J. Am. Chem. Soc.* 2005, **127**, 13120.
2 H. Zhang; J. Tang; Q. Zhang; G. Zhao; G. Yang; J. Zhang; O. Zhou; L. C. Qin, *Adv. Mater.* 2006, **18**, 87.
3 H. Zhang; Q. Zhang; J. Tang; L. C. Qin, *J. Am. Chem. Soc.* 2005, **127**, 8002.
4 H. Zhang; J. Tang; J. Yuan; J. Ma.; N. Shinya; K. Nakajima; H. Murakami; T. Ohkubo; L. C. Qin, *Nano lett.* 2010, **10**, 3539.
5 X. H. Ji; Q. Y. Zhang; J. Q. Xu; Y. M. Zhao, *Prog. Solid St. Chem.* 2011, **39**, 51.
6 J. Xu.; G. Hou.; H. Li.; T. Zhai.; B. Dong.; H. Yan.; Y. Wang.; B. Yu.; Y. Bando; D. Golberg., *NPG Asia Mater.* 2013, **5**, 53.
7 S. S.Warule; N. S. Chaudhari; B. B. Kale.; S. Pandiraj; R. T. Khare; M. A. More, *Cryst. Eng. Comm.* 2013, **15**, 890.
8 X. B. Li.; X. W. Wang; Q. Shen; J. Zheng; W. H. Liu.; H. Zhao; F. Yang; H. Q. Yang, *ACS Appl. Mater. & Inter.* 2013, **5**, 3033.
9 T. Zhai; X. Fang; Y. Bando; Q. Liao; X. Xu; H. Zeng; Y. Ma; J. Yao.; D. Golberg, *ACS Nano* 2009, **3**, 949.
10 X. Wang; Z. Lin; K. Qi; Z. Chen.; Z. Wang; Y. Jiang, *J. of Phy. D: Appl. Phy.* 2007, **40**, 4775.
11 M. Jha; R. Patra; S. Ghosh.; A. K. Ganguli, *J. Mater. Chem.* 2012, **22**, 6356.
12 D. J. Late; M. A. More; P. Misra; B. N. Singh; L. M. Kukreja; D. S. Joag, *Ultramicroscopy* 2007, **107**, 825.
13 D. J. Late; M. A. More; S. Sinha; K. Dasgupta; P. Misra; B. N. Singh; L. M. Kukreja; S. V. Bhoraskar; D. S. Joag, *Appl. Phy. A* 2011, **104**, 677.
14 D. J. Late; K. S. Date; M. A. More; P. Misra; B. N. Singh; L, M. Kukreja; C. V. Dharmadhikari; D, S. Joag, *Appl. Sur. Sci.* 2008, **254**, 3601.
15 L. Wang; L. Xu; Z. Ju; Y. Qian, *Cryst. Eng. Comm.* 2010, *12*, 3923.
16 J. Xu.; Y. Zhao; C. Zou, *Chem. Phy. Lett.* 2006, **423**, 138.
17 M. Deo; D. Shinde.; A. Yengantiwar; J. Jog; B. Hannoyer.; X. Sauvage; M. A. More; S. Ogale, *J. Mate.r Chem* 2012, **22**, 17055.
18 A. Paracchino, N. Mathews, T. Hisatomi, M. Stefik, S. D. Tilley and M. Grätzel, *Energy & Env. Sci.* 2012, **5**, 8673.
19 S. S. Warule; N. S. Chaudhari; B. B. Kale; K.R. Patil; P. M. Koinkar; M. A. More; Murakami, R., *J. Mater. Chem.* 2012, **22**, 8887.
20 D. R. Shinde,; P. G. Chavan; S. Sen.; D. S. Joag; M. A. More.; S. C. Gadkari; S. K. Gupta., *ACS Appl. Mater. & Inter.* 2011, **3**, 4730.
21 H. Shan.; C. Liu.; L. Liu.; J. Zhang.; H. Li.; Z. Liu.; X. Zhang.; X. Bo.; X. Chi., *ACS Appl.Mater. & Inter.* 2013, **5**, 6376-80.
22 N. Wang.; Y. H. Yang; J. Chen.; N. Xu.; G. Yang., *The J. of Phys. Chem. C* 2010, **114**, 2909.
23 S. S. Warule.; N. S. Chaudhari.; R. T. Khare.; J. D. Ambekar.; B. B. Kale.; M. A. More., *Cryst. Eng. Comm.* 2013, **15**, 7475.
24 X. Tang, G. Li and S. Zhou, *Nano Lett.* 2013, **13**, 5046-5050.
25 S. Poulston.; P. M. Parlett.; P. Stone.; M. Bowker., *Surf. and Inter. Anal.* 1996, **24**, 811-820.
26 R. K.Selvan.; I. Genish.; I. Perelshtein.; J. M. CalderonMoreno.; A. Gedanken., *J. of Phys. Chem. C* 2008, **112**, 1795.
27 A. J. Nelson.; J. J.Adams; K. I. Schaffers., *Appl. Surf. Sci.* 2005, **252**, 1228.
28 W. J. Lademan,; A. K. See,; L. E. Klebanoff,; G. van der Laan., *Phys. Rev. B* 1996, **54**, 17191.
29 D. Briggs., Handbook of X-ray Photoelectron Spectroscopy C. D. Wanger, W. M. Riggs, L. E. Davis, J. F. Moulder and G.

E.Muilenberg Perkin-Elmer Corp., Physical Electronics Division, Eden Prairie, Minnesota, USA, 1979. 190 pp. *Surf. and Inter. Analy.*1981, **3**,

30 D. J. Late.; M. A. More.; D. S. Joag.; P. Misra.; B. N. Singh.; L. M. Kukrej,. *Appl. Phy. Lett.* 2006, **89**, 123510.

31 R. H. Fowler,; L. Nordheim., *Proc. of the Ro. Soc. of London. Sr. A, Containing Papers of a Math. and Phy. Character* 1928, **119**, 173.

32 R. G. Forbes., *Nanotech.*2012, **23**, 095706.